

Large thermoelectric spin-valve effect with a superconductor

Pablo Tüero^{†,1}, Johanne Bratland Tjernshaugen^{†,2}, Carlos Sanchez,¹ César Gonzalez-Ruano,¹ Yuan Lu,³ Jacob Linder,^{2,*} and Farkhad G. Aliev^{4,†}

¹*Departamento Física de la Materia Condensada C-III, Universidad Autónoma de Madrid, Madrid 28049, Spain*

²*Center for Quantum Spintronics, Department of Physics,*

Norwegian University of Science and Technology, NO-7491 Trondheim, Norway

³*Université de Lorraine, CNRS, IJL, F-54000 Nancy, France*

⁴*Departamento Física de la Materia Condensada C-III,*

Instituto Nicolás Cabrera (INC) and Condensed Matter Physics Institute (IFIMAC), Universidad Autónoma de Madrid, Madrid 28049, Spain

Recent studies have revealed magnetically controllable thermoelectric effects in superconductor/ferromagnet (S/F) structures. A tunable cryogenic thermoelectric generator needs not only a high conversion factor between electricity and heat, but also a large change in the thermoelectric output when switching the magnetic state of the device. Here, we experimentally measure and numerically model thermoelectric effects in fully epitaxial F/S/F junctions based on commercially available, easily grown materials, as well as their dependence on the magnetic configuration of the F electrodes. We observe sizeable Seebeck coefficients for the parallel alignment of the ferromagnetic electrodes, reaching values of about $100 \mu\text{V}/\text{K}$. Importantly, we find a decrease of the thermoelectric signal of more than an order of magnitude when switching from a parallel to an antiparallel configuration, constituting a large thermoelectric spin-valve effect. Theoretical modeling based on a self-consistent non-equilibrium Keldysh-Usadel Green function theory, combined with micromagnetic simulations, qualitatively reproduce the experimental findings. These findings pave the way for the development of efficient and versatile cryogenic thermoelectric heat engines.

Introduction. – The conversion of heat into electricity and vice versa is known as thermoelectricity. This field of research has received increasing attention over the last decades, not only for the purpose of gaining insight into the fundamental physics of new materials [1, 2], but also due to the large number of industrial applications thermoelectricity enables. These include vastly different areas such as temperature control (cooling) of electronic devices, air conditioning, food refrigeration, and ultrasensitive detection of electromagnetic radiation [3–7].

A prominent challenge with thermoelectricity occurs in the low-temperature regime. Whereas conventional thermoelectric materials typically operate in the regime $100 \text{ K} - 400 \text{ K}$, their performance, in terms of for instance the Seebeck coefficient, drastically drops at lower temperatures [8]. Therefore, there exists a need to design better material platforms that can yield efficient thermoelectricity even under cryogenic conditions. One promising application lies in cryogenic cooling [9], which so far has been mainly dependent on liquid nitrogen which is both costly and requires regular refilling.

Superconducting materials have poor thermoelectric properties on their own. However, they become excellent thermoelectric materials when combined with ferromagnets [10, 11]. This emergent phenomenon has been predicted [12, 13] and subsequently experimentally confirmed [14]. The key mechanism behind this emergent thermoelectricity is a spin-dependent particle-hole asymmetry in a superconductor that coexists with a spin-splitting field, which in turn is utilized by using the spin-selective transport properties of ferromagnets. Combining superconductors with antiferromagnets also produces enhanced thermoelectric effects [15].

Very recently, it has been predicted [16] and experimentally demonstrated [17, 18] that interfacing a superconductor with

two ferromagnets allows the Seebeck coefficient of the system to be tuned via the magnetic alignment of the ferromagnetic regions. However, in order for such an effect to be viable for cryogenic thermoelectric applications, a number of conditions have to be met. Firstly, one would need to use commercially available materials with high spin polarization which are easily grown. Secondly, to maximize the temperature window of operation, one would need to use a superconductor that does not have a very low critical temperature T_c (like Al). Thirdly, the resulting magnitude of the thermoelectric effect would need to be sizeable at temperatures well below T_c at the same time as having a large difference in the Seebeck coefficient for the parallel (P) and antiparallel (AP) magnetic states of the spin-valve.

In this work, we report the experimental observation of a large superconducting thermoelectric spin-valve effect that meets all of the key criteria stated above. This represents a major advance compared to previous works on related superconductor/ferromagnet structures [17, 18]. Specifically, we study the spin-dependent transport and thermoelectric response in Fe/MgO/V/MgO/Fe/Co structures as a function of the relative alignment between the soft (Fe) and hard (Fe/Co) F electrodes. Our findings demonstrate a considerable thermoelectric effect, with a Seebeck coefficient exceeding $100 \mu\text{V}/\text{K}$ at base temperatures around $0.1T_c$. Importantly, we report a large change in the thermoelectric response – greater than a factor of 10 – when switching the device from the antiparallel (AP) to the parallel (P) alignment of the electrodes. Analyzing the results, we find a high sensitivity of the thermoelectric response to magnetic domain rotation and motion, as highlighted by the comparison of experimental thermoelectric and magnetoresistance data with micromagnetic simulations and theoretical

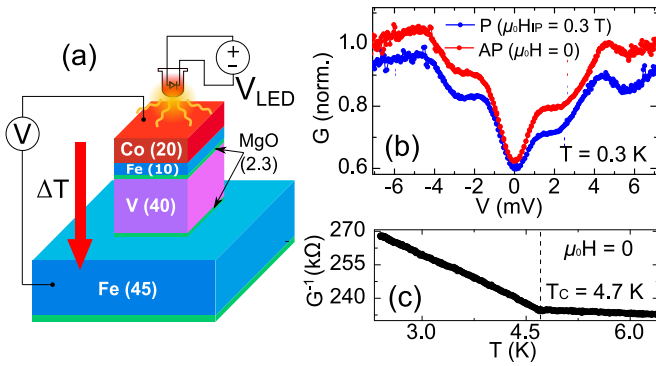


FIG. 1. (a) Sketch of the F/S/F junctions when heated by a LED. Layer thickness is given in nm. (b) Conductance–bias curves under different magnetic configurations measured at $T = 0.07T_c$. Conductance is normalized so that $G(V = 7 \text{ mV}) = 1$ when $\mu_0 H = 0$. (c) Temperature dependence of the zero bias resistance (G^{-1}) measured at $V = \pm 0.1 \text{ mV}$ with $\mu_0 H = 0$, showing a superconducting critical temperature of 4.7 K indicated by the dashed line. The increase in resistance below T_c corresponds to the opening of a partial gap in the conductance due to superconductivity.

modeling based on the non-equilibrium Keldysh-Usadel Green function formalism.

Experimental results. – Figure 1(a) illustrates the experimental setup and the specific junctions under study. We measured magnetoresistance (MR) and thermoelectric (TE) effects in epitaxial Fe(45)/MgO(2.3)/V(40)/MgO(2.3)/Fe(10)/Co(20) junctions grown on MgO(001) substrates, with layer thicknesses provided in nanometers. Further details on junction growth, characterization, experimental setup, and simulation procedures are available in the Supplemental Material [19]. In these F1/S/F2 junctions, V is the BCS superconductor (S), Fe serves as the soft magnetic electrode (F1) and Fe/Co functions as the magnetically hard electrode (F2), while the MgO acts as a symmetry-filtering tunnel barrier, facilitating high spin polarization (P) in Fe, exceeding 0.7–0.8 [20, 21]. Due to the weak antiferromagnetic coupling of the junctions [22–25], two distinct magnetic states are experimentally observed: at low fields, the junctions tend toward an antiparallel alignment, while a moderate field of 0.1–0.2 T will drive them into a parallel magnetic state. Figure 1(b) provides a low-bias electron transport characterization of the junctions in the superconducting state for both magnetic alignments, and Figure 1(c) provides temperature-dependent subgap conductance measurements that show a relatively high critical temperature for the vanadium superconductor, exceeding 4.5 K.

Figure 2(a) presents our main experimental observation: a substantial (over 10 \times) change in the TE voltage between the AP and P alignments of the ferromagnetic electrodes. The Seebeck coefficient for the parallel alignment, calculated based on numerically evaluated temperature gradients [19], reaches a considerable value of approximately 100 $\mu\text{V}/\text{K}$. The strong magnetic field dependence of the TE signal disappears above T_c . Remarkably, as the magnetic field decreases and the magnetic

configuration transitions from the P to AP state, the TE signal changes relatively smoothly. In contrast, the transition from AP to P with increasing in-plane magnetic field leads to an abrupt increase in the TE response, accompanied by a subtle but reproducible “overshoot” effect manifested as a peak followed by an immediate drop, shown in detail in Figure 2(b). As discussed below, this peak may correspond to a rapid change in the magnetization configuration of the F electrodes due to the combined effects of macrospin rotation and domain wall formation and displacement. Magnetoresistance measurements [Figure 2(c)] performed during the TE experiments further support this abrupt transition in the magnetization configuration when the P state is reached from the AP state, albeit without the distinct “overshoot” in the MR signal. We observe that the MR remains qualitatively similar above and below T_c , but it increases by approximately a factor of three in the superconducting state. This indicates that the spin signal is more effectively transferred between the two Fe electrodes through the 40 nm thick V layer when vanadium enters the superconducting state, which is possibly due to the generation of superconducting spin-triplet states [21, 26]. Figure 2(d) illustrates the TE response as a function of the temperature gradient at various fixed magnetic fields, color-coded to correspond with the MR plot in Figure 2(c), confirming a strong dependence of the TE response with the magnetic state of the junctions.

Micromagnetic simulations. – Numerical simulations of the TE response require knowledge about the average angle between the magnetizations of the two ferromagnets enclosing the superconductor. This information was obtained through micromagnetic simulations using the open-source software MuMax³ [27]. At the same time, in order to mimic the experimental setup of Figure 1(a), the system was divided into three different regions. Region 1 models the soft 45 nm thick Fe layer, while region 2 is the 10 nm thick Fe layer and Region 3 the 20 nm thick Co layer, that together form the hard Fe/Co electrode (see [19] for simulation details). To simulate a more realistic system, the presence of defects in the crystalline structure of the layers was taken into account. A concentration of 25% for superficial and 10% for bulk defects was considered. [19].

Moreover, owing to the presence of the low field antiferromagnetic coupling (AF) coupling between the two F layers, a negative exchange interaction was introduced between regions 1 and 2 by means of a negative Ruderman–Kittel–Kasuya–Yosida coupling constant (RKKY). Different RKKY constants from $-0.5 \text{ mJ}/\text{m}^2$ to $-2 \text{ mJ}/\text{m}^2$ were considered. The simulations were performed by varying the magnetic field starting from -0.5 T and up to 0.5 T . The results for the angle difference $\Delta\theta(H)$ in Figure 3(a) and Figure 4(c) were computed based on the macrospin of each region. That means that the average magnetization vector for regions 1 and 2 was computed separately, and then the angle between them was calculated.

To calculate the MR we followed a simplified model [28] to approximate the magnetic state dependent conductance G for our junctions (see [19] for details). We simulated the MR using two approaches. The first one (Av.Angle) calculates

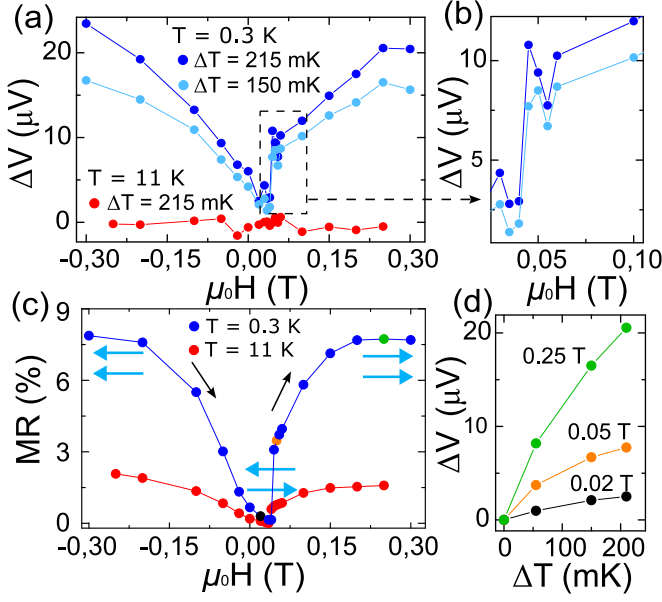


FIG. 2. Thermoelectric response of a F/S/F junction as a function of the applied in-plane (IP) magnetic field at $T = 0.3$ K and two different evaluated ΔT values. For comparison, a much smaller thermoelectric response observed above the critical temperature (at $T = 11$ K) is also shown. Part (b) zooms the low field region in (a), where an abrupt transition from the AP to the P state takes place. (c) Typical magnetoresistance (MR) curves vs IP magnetic field at a bias of $V = 5$ mV at $T = 0.3$ K and 11 K. The blue arrows show the relative magnetic alignment of the ferromagnetic electrodes while the black arrow shows the direction of variation of magnetic field. (d) Dependence of the TE response on the evaluated temperature difference between the ferromagnetic electrodes, measured at different IP magnetic states as indicated by the colored points in (c).

conductance as a function of the angle of the averaged magnetization in the two layers. The second approach divides the magnetic layers into a number of interfacial cells and then averages the conductance between each cell (discretization size of $2.34 \times 2.34 \times 1.67$ nm³ was used, see [19] for the details) from the one electrode and a randomly chosen cell of the opposite electrode. Then, the electrodes were interchanged and same procedure was repeated. The second method (Rnd.Diff.) thus models elastic impurity scattering of the electrons within the 40nm thick V layer separating the ferromagnetic electrodes. As one observes in Figure 3(b), using the lowest AF coupling value of RKKY = -0.5 mJ/m², the above mentioned concentration of defects and the Rnd.Diff. method, we obtain a MR curve which is qualitatively similar to the experimental measurements in Figure 2(c). The magnetoresistance saturates below 0.3 T and the “overshoot” effect is reduced as in MR experiments.

Thermoelectricity via non-equilibrium Green functions. – We model the thermoelectric effect in the system shown in Figure 4(a). The ferromagnets are modeled as normal reservoirs with spin-active interfaces, and the relative angle between the average in-plane magnetizations of the interfaces is given by $\Delta\theta$. In such mesoscopic superconducting hybrid systems,

the non-equilibrium quasiclassical Keldysh-Usadel formalism [10, 29, 30] is known to compare well with experiments. The 8×8 quasiclassical and isotropic Green function \check{g} in Keldysh \otimes Nambu \otimes spin space can be calculated in the diffusive limit from the Usadel equation [29],

$$\frac{\partial}{\partial(x/\xi)} \left(\check{g} \frac{\partial \check{g}}{\partial(x/\xi)} \right) = -i[\varepsilon \hat{\tau}_3 \otimes \hat{\sigma}_0 + \hat{\Delta}, \check{g}] / \Delta_0. \quad (1)$$

Here, ξ is the superconducting coherence length, ε is the energy relative to the Fermi level, and Δ_0 is the bulk superconducting gap. The self-energy $\hat{\Delta} = \text{antidiag}(\Delta, -\Delta, \Delta^*, -\Delta^*)$ depends on the superconducting order parameter Δ , which in turn can be calculated from the Green function as

$$\frac{\Delta}{\Delta_0} = -\frac{N_0 \lambda}{4} \int_{-\omega_c}^{\omega_c} \check{g}_{23}^K \left(\frac{\varepsilon}{\Delta_0} \right) d \left(\frac{\varepsilon}{\Delta_0} \right). \quad (2)$$

Therefore, the Usadel equation must be solved self-consistently for the order parameter. To this end, we perform fixed-point iterations for both the magnitude $|\Delta|$ of the order parameter $\Delta = |\Delta|e^{i\phi}$ and its phase gradient $\partial_x \phi$, which both are physical observables. In eq. (2), N_0 is the normal-state density of states at the Fermi level and λ is the coupling constant. The cutoff energy $\omega_c = \cosh(1/N_0 \lambda)$ for the equation to be consistent.

The interfaces to the ferromagnets are modeled by spin-active boundary conditions [31, 32]. These are characterized by a conductance G_0 , the length l of the superconductor, a polarization P , a spin-mixing G_φ , and the average interface magnetization direction \mathbf{m} . The numerical values $G_0/G = 1/3.5$ with G the bulk conductance, $l = 1.5\xi$ and $P = 0.8$ are chosen to match the experimental values, while the spin-mixing angle is typically taken to be a fitting parameter and is set to $G_\varphi/G_0 = 2.75$. The ferromagnets themselves are treated as non-superconducting metallic reservoirs at temperatures $0.07T_c$ and $0.12T_c$ for the soft (MgO-Fe) and hard (Fe-Co) ferromagnets, respectively. The thermovoltage ΔV is found by solving the root-finding problem $I(\Delta V) = 0$, where the current I is calculated from the Green function after solving the Usadel equation. Figure 4(b) shows the thermovoltage as a function of the angle difference $\Delta\theta$. We use micromagnetic simulations for four different RKKY couplings, as shown in Figure 4(c), to model the thermoelectric response to an applied magnetic field. The thermovoltage as a function of the applied magnetic field is presented in Figure 4(d), and does qualitatively match the experimental data in Figure 2(a). The difference in magnitude of the thermovoltage between the simulations and measurements may be attributed to the restriction in quasiclassical theory regarding how the reservoirs are treated. Normal and ferromagnetic reservoirs are described by the same Green function due to the requirement of a weak spin polarization in the quasiclassical approximation, unlike the strongly polarized ferromagnet Fe used in the experiment, and this likely reduces the numerically simulated value for ΔV . No such methodology restriction applies to the interfacial polarization in our treatment, however, which can model strongly polarized ferromagnetic interfaces [31].

Discussion. – Our experimental results demonstrate that the magnetic configuration of the superconducting spin-valve

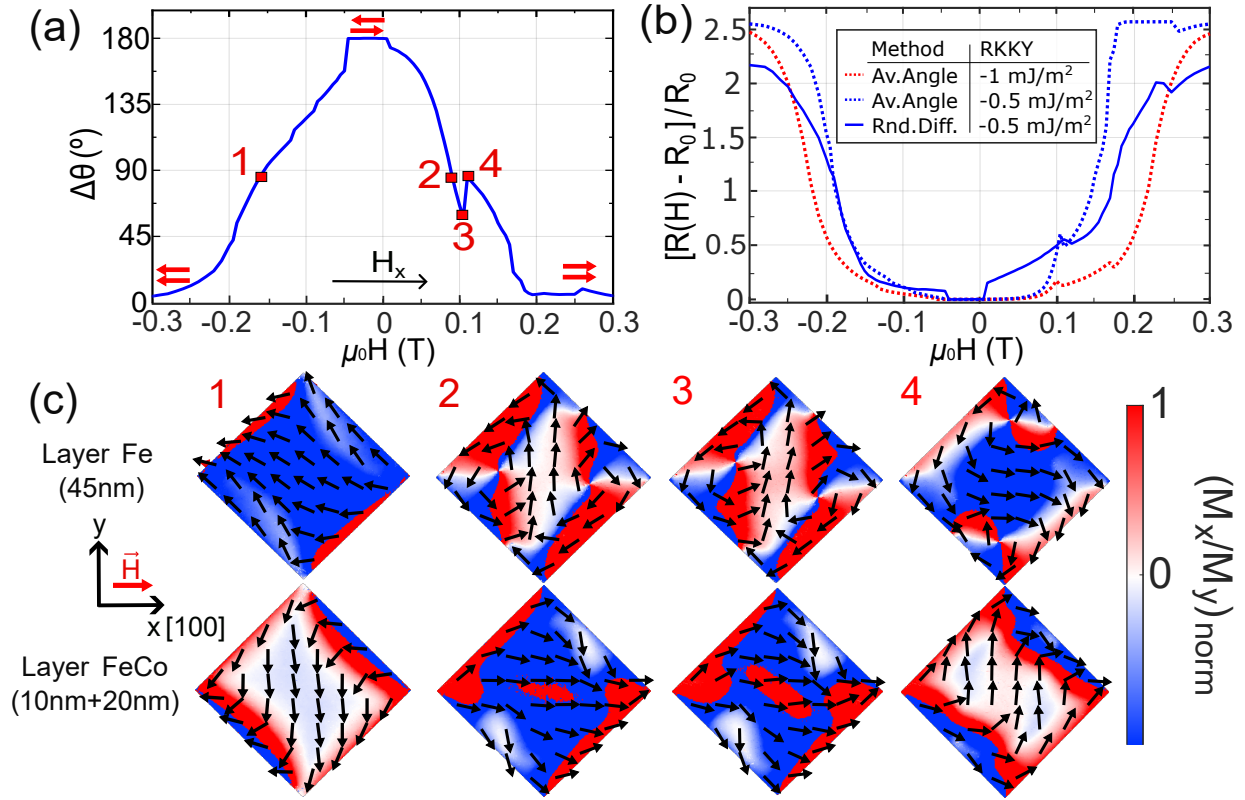


FIG. 3. (a) Angle difference between the macrospin of the two F regions for an AF coupling of RKKY = -0.5 mJ/m² (selected points pointed with numbers). (b) Normalized magnetoresistance for two different couplings and calculated using two methods explained in the text, where R_0 is the resistance at $\mu_0 H = 0$. (c) Magnetization map for the interface of both F layers on the selected points in (a).

changes the thermoelectric signal by more than an order of magnitude when switching from a parallel to an antiparallel state. After achieving a qualitative agreement between the experimental results and simulations of both the TE and MR effects, we conclude that the thermoelectric effects are highly sensitive to the collective domain rotation within the ferromagnetic layers, as shown in Figure 3(c). At $H = 0$, due to the negative exchange interaction, the layers tend to align in an antiparallel configuration, resulting in the observed minima in resistance and TE signals. When an in-plane magnetic field is applied along one of the easy axes, the reorientation of the magnetization in the two ferromagnetic layers involves complex magnetic dynamics, including the formation of inner and edge domain walls, as illustrated in Figure 3(c). Due to the magnetocrystalline anisotropy, magnetic dipoles preferentially align towards the crystal's easy axes as exemplified by Figure 3(c). In Figure 3(c), we also observe how the correlated rotation between the two ferromagnetic layers can induce an “overshoot” in the TE response due to the sharp dip that occurs in the angle misalignment between the average magnetizations in Figure 3(a). For instance, at the selected point 3, one layer is mainly aligned along the y -axis, while the other aligns along the x -axis. At point 4, the alignment is reversed. This abrupt shift in alignment was consistently observed in several simulations.

Following this transition, the system adopts a configuration almost equivalent to point 1 in the negative part of the sweep, and the layers continue to rotate towards a parallel alignment at high fields. This shows the asymmetry between the $P \rightarrow AP$ transition with respect to the $AP \rightarrow P$.

Conclusions. – We report the experimental observation of a large superconducting thermoelectric spin-valve effect which meets a number of key criteria required for cryogenic thermoelectric applications: (i) we use commercially available materials with high spin polarization which are easily grown; (ii) a considerable thermoelectric effect, with a Seebeck coefficient exceeding $100 \mu\text{V/K}$, (iii) a large change in the thermoelectric response – greater than a factor of 10 – when switching the device from AP to P alignment. Micromagnetic simulations and theoretical modeling based on the non-equilibrium Keldysh-Usadel Green function formalism are consistent with both the thermoelectric and magnetoresistance results.

Acknowledgments. The work in Madrid was supported by Spanish Ministry of Science and Innovation (PID2021-124585NB-C32 and TED2021-130196B-C22). F.G.A. also acknowledges financial support from the Spanish Ministry of Science and Innovation through the María de Maeztu Programme for Units of Excellence in R&D (CEX2018-000805-M). The work in Trondheim was supported by the Research Coun-

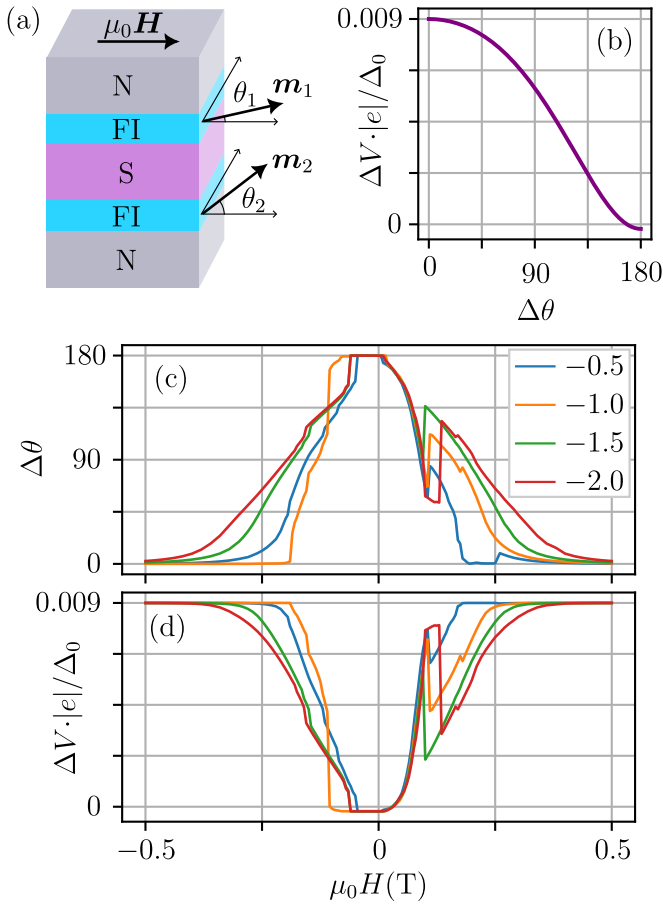


FIG. 4. (a) The model used in the numerical calculations. The superconductor S is sandwiched between two ferromagnets, modelled as normal reservoirs N with spin-active interfaces FI. The angle difference between the average in-plane magnetizations m_1 and m_2 of the interfaces is given by $\Delta\theta = \theta_2 - \theta_1$. The external magnetic field $\mu_0\mathbf{H}$ affects m_1 and m_2 differently. (b) Induced thermovoltage ΔV as a function of the angle difference. $\Delta_0/|e|$ is typically of the order 1 mV. (c) Simulated angle difference for an external magnetic field μ_0H with four different RKKY couplings in units mJ/m^2 . (d) Thermovoltage as a function of the external magnetic field.

cil of Norway through Grant No. 323766 and its Centres of Excellence funding scheme Grant No. 262633 “QuSpin.” Support from Sigma2 - the National Infrastructure for High Performance Computing and Data Storage in Norway, project NN9577K, is acknowledged.

[†]P.T. and J.B.T. contributed equally to the manuscript.

* e-mail: jacob.linder@ntnu.no

[†] e-mail: farkhad.aliev@uam.es

- [1] F. G. Aliev, V. V. Kozyrkov, V. V. Moshchalkov, R. V. Skolozdra, and K. Durcewski, *Zeit. Phys. Cond. Mat.* **80**, 353 (1990).
 [2] A. Ojha, R. K. Sabat, and S. Bathula, *Mater. Sci. Semicond. Process.* **171**, 107996 (2024).

- [3] T. M. Tritt, *Ann. Rev. Mat. Research* **41**, 433 (2011).
 [4] J. Wei, L. Yang, Z. Ma, P. Song, M. Zhang, J. Ma, F. Yang, and X. Wang, *J. Mat. Sci.* **55**, 12642 (2020).
 [5] Z. Soleimani, S. Zoras, B. Ceranic, S. Shahzad, and Y. Cui, *Sustainable Energy Technologies and Assessments* **37**, 100604 (2020).
 [6] X.-L. Shi, J. Zou, and Z.-G. Chen, *Chem. Rev.* **120**, 7399 (2020).
 [7] S. Irfan, Z. Yan, and S. B. Khan, *Materials Science for Energy Technologies* **7**, 349 (2024).
 [8] J. Feng, J. Li, and R. Liu, *Nano Energy* **126**, 109651 (2024).
 [9] S. R. Harutyunyan, V. H. Vardanyan, A. S. Kuzanyan, V. R. Nikoghosyan, S. Kunii, K. S. Wood, and A. M. Gulian, *Applied Physics Letters* **83**, 2142 (2003).
 [10] F. S. Bergeret, M. Silaev, P. Virtanen, and T. T. Heikkilä, *Rev. Mod. Phys.* **90**, 041001 (2018).
 [11] T. Heikkilä, M. Silaev, M. Virtanen, and F. S. Bergeret, *Prog. Surf. Sci.* **94**, 100540 (2019).
 [12] P. Machon, M. Eschrig, and W. Belzig, *Phys. Rev. Lett.* **110**, 047002 (2013).
 [13] A. Ozaeta, P. Virtanen, F. S. Bergeret, and T. T. Heikkilä, *Phys. Rev. Lett.* **112**, 057001 (2014).
 [14] S. Kolenda, M. J. Wolf, and D. Beckmann, *Phys. Rev. Lett.* **116**, 097001 (2016).
 [15] P. O. Sukhachov, E. W. Hodt, and J. Linder, *Phys. Rev. B* **110**, 094508 (2024).
 [16] J. A. Ouassou, C. González-Ruano, D. Caso, F. G. Aliev, and J. Linder, *Phys. Rev. B* **106**, 094514 (2022).
 [17] C. González-Ruano, D. Caso, J. A. Ouassou, C. Tiusan, Y. Lu, J. Linder, and F. G. Aliev, *Phys. Rev. Lett.* **130**, 237001 (2023).
 [18] C. I. L. de Araujo, P. Virtanen, M. Spies, C. Gonzalez-Orellana, M. I. Kerschbaumer, C. Rogero, T. T. Heikkilä, F. Giazotto, and E. Strambini, *Nat. Commun.* **15**, 4823 (2024).
 [19] (See Supplemental Material for additional details on the micro-magnetic simulations, quasiclassical modelling of the thermoelectric signal, and experimental characterization of the samples.)
 [20] I. Martínez, C. Tiusan, M. Hehn, M. Chshiev, and F. G. Aliev, *Scientific Reports* **8**, 9463 (2018).
 [21] C. González-Ruano, L. G. Johnsen, D. Caso, C. Tiusan, M. Hehn, N. Banerjee, J. Linder, and F. G. Aliev, *Phys. Rev. B* **102**, 020405 (2020).
 [22] B. Kochelaev, L. Tagirov, and M. Khusainov, *Zh. Eksp. Teor. Fiz.* **76**, 578 (1979).
 [23] M. Khusainov, *Zh. Eksp. Teor. Fiz.* **109**, 524 (1996).
 [24] A. Di Bernardo, S. Komori, G. Livanas, G. Divitini, P. Gentile, M. Cuoco, and J. W. A. Robinson, *Nature Materials* **18**, 1194–1200 (2019).
 [25] P. Tuero, C. González-Ruano, Y. Lu, C. Tiusan, and F. G. Aliev, *Phys. Rev. B* **110**, 094504 (2024).
 [26] I. Martínez, P. Högl, C. González-Ruano, J. P. Cascales, C. Tiusan, Y. Lu, M. Hehn, A. Matos-Abiague, J. Fabian, I. Žutić, and F. G. Aliev, *Phys. Rev. Appl.* **13**, 014030 (2020).
 [27] A. Vansteenkiste, J. Leliaert, M. Dvornik, M. Helsen, F. García-Sánchez, and B. V. Waeyenberge, *AIP Advances* **4**, 107133 (2014).
 [28] J. C. Slonczewski, *Phys. Rev. B* **39**, 6995 (1989).
 [29] K. D. Usadel, *Phys. Rev. Lett.* **25**, 507 (1970).
 [30] W. Belzig, F. K. Wilhelm, C. Bruder, G. Schön, and A. D. Zaikin, *Superlattices Microstruct.* **25**, 1251 (1999).
 [31] M. Eschrig, A. Cottet, W. Belzig, and J. Linder, *New J. Phys.* **17**, 083037 (2015).
 [32] J. A. Ouassou, T. D. Vethaak, and J. Linder, *Phys. Rev. B* **98**, 144509 (2018).

Supplemental Material for *Large thermoelectric spin-valve effect with a superconductor*

Pablo Tuero,^{1,2} Johanne Bratland Tjernshaugen,^{3,2} Carlos Sanchez,¹ César Gonzalez-Ruano,¹ Yuan Lu,⁴ Jacob Linder,^{3,*} and Farkhad G. Aliev^{5,†}

¹*Departamento Física de la Materia Condensada C-III, Universidad Autónoma de Madrid, Madrid 28049, Spain*

²*These authors contributed equally to the manuscript*

³*Center for Quantum Spintronics, Department of Physics, Norwegian University of Science and Technology, NO-7491 Trondheim, Norway*

⁴*Université de Lorraine, CNRS, IJL, F-54000 Nancy, France*

⁵*Departamento Física de la Materia Condensada C-III, Instituto Nicolás Cabrera (INC) and Condensed Matter Physics Institute (IFIMAC), Universidad Autónoma de Madrid, Madrid 28049, Spain*

(Dated: February 12, 2025)

I. SAMPLE GROWTH AND EXPERIMENTAL PROCEDURE

The F/S/F junctions under study are grown by molecular beam epitaxy (MBE) with their crystalline quality controlled by in-situ RHEED measurements. The structures are lithographed into $20 \times 20 \mu\text{m}^2$ lateral size samples. A more detailed description of the growth process can be found in Ref. [1].

Magnetoresistance (MR) and thermoelectric (TE) response measurements are performed inside a Janis He³ cryostat at a base temperature of 0.3 K. For both kinds of measurements, the voltage drop through the sample V is measured at a given applied current I with a four-point probe set up. The magnetic field H is applied along the easy axis of the samples. To evaluate the MR, the voltage is measured at currents $I = \pm 10$ nA, so that the resistance is calculated as $R = V/(2|I|)$. The TE response experiments are performed with the use of a commercial Light Emitting Diode (LED), in a similar way as explained in Ref. [2]. The voltage V_{LED} is supplied by a SRS-DC205 voltage source to a LED placed above the samples. By controlling V_{LED} one can tune the power that the diode dissipates, creating a temperature gradient ΔT across the junctions. A TE measurement at a given V_{LED} is carried out as follows. First, forcing $I = 0$ through the sample at 0.3 K, the voltage across the sample (V_{OFF}) is measured while $V_{LED} = 0$. Then, the target V_{LED} is applied and after two seconds the voltage across the junctions is again measured (V_{ON}). The TE voltage is then $\Delta V(V_{LED}) = V_{ON} - V_{OFF}$. The background voltage is removed as done in Ref. [2]. The estimation of ΔT as a function of V_{LED} in order to compute $\Delta V(\Delta T)$ is discussed in the following section.

II. MODELING OF THE TEMPERATURE PROFILE

The temperature gradient across the junctions under different values of V_{LED} was modeled with COMSOL [3] simulations. First, the room temperature $I - V$ curve of the diode provided by the manufacturer (model LUXEON 3030 2D) is re-scaled to match the working range of the LED at low temperatures. Then, for a given V_{LED} the power dissipated by the device is $W = I \times V_{LED}$, and the power per unit area that reaches the junctions top surface (distance between LED and sample ~ 1 cm) is

$$w = \frac{I \times V_{LED}}{4\pi \text{ cm}^2} [\text{W}/\text{cm}^{-2}]. \quad (1)$$

Thus, the total heat flux entering the sample through the top surface would be

$$h = \frac{I \times V_{LED}}{4\pi \times 10^2} [\text{W}], \quad (2)$$

where we are assuming that the LED is heating the area of the gold contact atop the samples (1 mm^2), and that all the heating power that reaches the contact is transmitted into the top layer of the sample. We use tabulated values for the different material parameters [4–7]. Importantly, the top MgO barrier is expected to be ~ 4 times more transparent than the bottom one [8], so

* e-mail: jacob.linder@ntnu.no

† e-mail: farkhad.aliev@uam.es

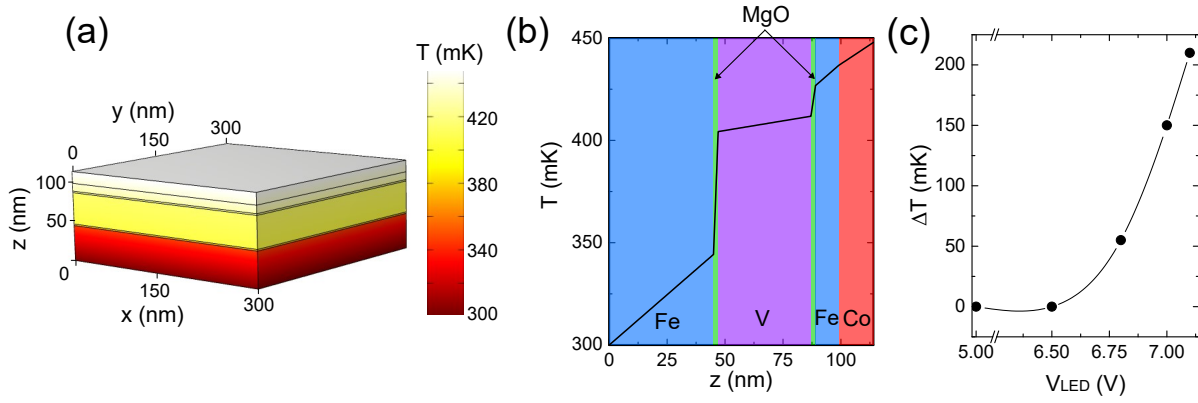


FIG. S1. (a) 3D model of the temperature distribution in the F/S/F junction with $V_{LED} = 7.0$ V. (b) Temperature profile along the vertical direction of the temperature distribution shown in (a). The different colored areas indicate the distinct material layers of the junction. We define ΔT as the temperature difference between the top and bottom most layers of the junction. (c) ΔT as a function of V_{LED} calculated for the V_{LED} values relevant to the experiment.

we have proportionally tuned its thermal conductivity. Steady state simulations are performed by constructing the junctions geometry, imposing an inward heat flux through the top surface given by eq. (2), assuming that the lateral faces of the stack are thermally isolated (the samples are in a vacuum) and fixing the temperature of the bottom surface to 0.3 K, since it is in contact with the cryostat's thermal bath. The simulation is repeated for every value of V_{LED} under consideration, with results for $V_{LED} = 7.0$ V shown in Fig.S1.(a) and (b). ΔT is defined as the temperature difference between the top and bottom faces of the sample, so it would be ~ 150 mK in Fig.S1.(b). The final results for ΔT vs V_{LED} are shown in Fig.S1.(c). The above definitions are conservative, as to provide an upper limit for ΔT in order to get a reasonable lower limit for the Seebeck coefficient.

III. MICROMAGNETIC SIMULATIONS METHODS

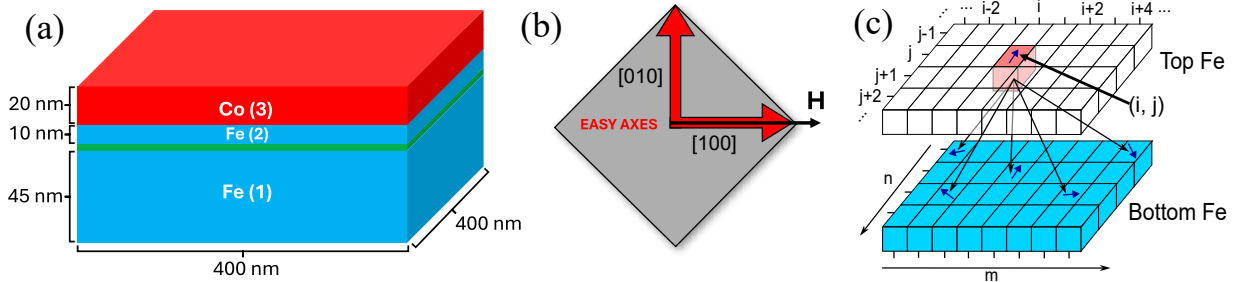


FIG. S2. (a) Sketch of the ferromagnetic junctions used in micromagnetic simulations. (b) Indications of the cubic magnetocrystalline anisotropy of the system and direction of the in-plane magnetic field applied. (c) Sketch describing the Rnd.Diff. method of magnetoresistance calculation.

The micromagnetic simulations are performed in MuMax³, and the simulated system is presented in Figure S2(a,b). It consists of a $400 \times 400 \times 75$ nm cuboid with a discretisation cell size of $2.34 \times 2.34 \times 1.67$ nm, smaller than exchange lengths for Fe and Co. The system is divided into three separated regions with different magnetic parameters and couplings between them to mimic the experimental setup in Fig. 1(a). All these regions have a base of 400×400 nm. To simulate a more realistic system, the presence of defects in the crystalline structure of the layers is taken into account. We make a distinction between two types of defects. First, superficial defects are only implemented in the first and last cell layers in Regions 1 and 3, and present a lower saturation magnetization than the normal material ($M_S^{\text{defect}} = 0.6M_S$). Second, bulk defects are introduced by adding disorder to the local magnetocrystalline anisotropy. To do that, the cells modelling bulk defects have a randomly distributed anisotropy direction and a change in the 1st order cubic anisotropy constant, in the range of $(1 \pm 0.15)K_1$. In this paper we use $K_1 = 4.8 \cdot 10^4$ J/m³ [9]. In the same way, the principal easy axes of magnetization are set to [100] and [010], as indicated in Figure S2(b).

To calculate the magnetoresistance we follow a simplified model [10] to approximate the magnetic state dependent conductance

G for our junctions with the following expression:

$$G = G_0(1 - P^2 \cos \Delta\theta). \quad (3)$$

Here, G_0 is the low bias conductance of the junctions in a perpendicular state, P is the effective spin polarization, and $\Delta\theta$ is the angle between the magnetizations of the ferromagnets.

For these calculations, we only take into consideration the interfacial layers of cells between regions 1 and 2. We consider two possible ways of calculating the total resistance G^{-1} of the junction. One (Av.Angle) method consists of direct application of Eq.(3) using the averaged magnetization angles between the regions. The second (Rnd.Diff.) considers every cell (i, j) of region 1 and calculates, using eq. (3), the conductance to a randomly chosen cell (n, m) in region 2 as sketched in Figure S2(c). Finally, we sum the contribution from all pairs in parallel to obtain the total conductance and resistance for the junction. We have verified that the resulting conductance does not change when the top and bottom Fe regions (1 and 2) are interchanged. Several repetitions of the Rnd.Diff. MR calculation method have been also carried out to verify robustness of the Rnd.Diff. method.

IV. SELF-CONSISTENT NON-EQUILIBRIUM KELDYSH-USADEL GREEN FUNCTION THEORY

The 8×8 Green function \check{G} in Keldysh \otimes Nambu \otimes spin space is defined as

$$\check{G} = \begin{pmatrix} \hat{G}^R & \hat{G}^K \\ 0 & \hat{G}^A \end{pmatrix}. \quad (4)$$

Here, the retarded Green function \hat{G}^R , the advanced Green function \hat{G}^A and the Keldysh Green function \hat{G}^K are defined in terms of the spinor

$$\psi(\mathbf{r}, t) = \left(\psi_\uparrow(\mathbf{r}, t) \quad \psi_\downarrow(\mathbf{r}, t) \quad \psi_\uparrow^\dagger(\mathbf{r}, t) \quad \psi_\downarrow^\dagger(\mathbf{r}, t) \right)^T, \quad (5)$$

as

$$\begin{aligned} \hat{G}^R(\mathbf{r}, t, \mathbf{r}', t') &= -i\theta(t - t')\hat{\rho}_4\{\psi(\mathbf{r}, t), \psi^\dagger(\mathbf{r}', t')\}, \\ \hat{G}^A(\mathbf{r}, t, \mathbf{r}', t') &= +i\theta(t' - t)\hat{\rho}_4\{\psi(\mathbf{r}, t), \psi^\dagger(\mathbf{r}', t')\}, \\ \hat{G}^K(\mathbf{r}, t, \mathbf{r}', t') &= -i\hat{\rho}_4\langle[\psi(\mathbf{r}, t), \psi^\dagger(\mathbf{r}', t')]\rangle. \end{aligned}$$

ψ_σ^\dagger and ψ_σ are the electronic creation and annihilation operators, respectively. The matrix $\hat{\rho}_4$ is a part of a set of matrices $\{\hat{\rho}_n\}$ that span the block-diagonal Nambu \otimes spin space,

$$\hat{\rho}_0 = \begin{pmatrix} \sigma_0 & 0 \\ 0 & \sigma_0 \end{pmatrix} \quad \hat{\rho}_1 = \begin{pmatrix} \sigma_1 & 0 \\ 0 & \sigma_1 \end{pmatrix} \quad \hat{\rho}_2 = \begin{pmatrix} \sigma_2 & 0 \\ 0 & \sigma_2 \end{pmatrix} \quad \hat{\rho}_3 = \begin{pmatrix} \sigma_3 & 0 \\ 0 & \sigma_3 \end{pmatrix} \quad (6)$$

$$\hat{\rho}_4 = \begin{pmatrix} \sigma_0 & 0 \\ 0 & -\sigma_0 \end{pmatrix} \quad \hat{\rho}_5 = \begin{pmatrix} \sigma_1 & 0 \\ 0 & -\sigma_1 \end{pmatrix} \quad \hat{\rho}_6 = \begin{pmatrix} \sigma_2 & 0 \\ 0 & -\sigma_2 \end{pmatrix} \quad \hat{\rho}_7 = \begin{pmatrix} \sigma_3 & 0 \\ 0 & -\sigma_3 \end{pmatrix}. \quad (7)$$

The exact Green function \check{G} can in principle be determined from the Gorkov equation [11], but in practice this is too hard and one relies on simplifying approximations for all but the simplest systems. In the quasiclassical limit, all energy scales in the system are much smaller than the Fermi energy and \check{G} is strongly peaked near the Fermi momentum \mathbf{p}_F [12, 13]. The quasiclassical Green function $\check{\Gamma}$ is found by constricting the Green function to the Fermi surface,

$$\check{\Gamma} \left(\varepsilon, \frac{\mathbf{p}_F}{|\mathbf{p}_F|} \right) = \frac{i}{\pi} \int_{-\omega_c}^{\omega_c} \check{G}(\varepsilon, \mathbf{p}) d\varepsilon_{\mathbf{p}}, \quad (8)$$

where $\varepsilon_{\mathbf{p}} = (|\mathbf{p}|^2 - |\mathbf{p}_F|^2)/2m$, and ε is measured relative to the Fermi energy. The quasiclassical Green function obeys the Eilenberger equation [14]. For diffusive systems where the elastic mean free path is much smaller than any other length scale in the system except the Fermi wavelength, the Eilenberger equation can be reduced to a diffusion-like equation. This is known as the Usadel equation [15],

$$\frac{\partial}{\partial(x/\xi)} \left(\check{g} \frac{\partial \check{g}}{\partial(x/\xi)} \right) = -i[\varepsilon\hat{\rho}_4 + \hat{\Delta}, \check{g}]/\Delta_0. \quad (9)$$

Here, \check{g} is the isotropic, quasiclassical Green function, which we term the Green function. The superconducting coherence length is ξ , and $\hat{\Delta} = \text{antidiag}(\Delta, -\Delta, \Delta^*, -\Delta^*)$ is a self-energy describing superconductivity in the system. The superconducting

order parameter is defined as $\Delta(\mathbf{r}) = -\lambda\langle\psi_{\downarrow}(\mathbf{r})\psi_{\uparrow}(\mathbf{r})\rangle$. Inelastic scattering in the Usadel equation is modeled using the Dynes approximation $\varepsilon \rightarrow \varepsilon + i\delta$. The retarded and advanced Green functions are related by $\hat{g}^A = -\hat{\rho}_4(\hat{g}^R)^\dagger\hat{\rho}_4$. The Keldysh Green function is related to those by

$$\hat{g}^K = \hat{g}^R\hat{h} - \hat{h}\hat{g}^A, \quad (10)$$

where $\hat{h} = h_n\hat{\rho}_n$ is the distribution function. Therefore, it is sufficient to determine the retarded Green function and the distribution function when solving the Usadel equation.

The non-equilibrium modes h_n in the distribution function describes the relation between occupation of electron and hole states with different spins. Holes are defined as missing electrons, and the hole has opposite spin to the missing electron. The distribution function can be rewritten in terms of the electron and hole occupation probabilities $f_{e,\sigma}$ and $f_{h,\sigma}$ as [16]

$$\hat{h} = \hat{1} - 2 \cdot \text{diag}(f_{e,\uparrow}, f_{e,\downarrow}, f_{h,\downarrow}, f_{h,\uparrow}). \quad (11)$$

In equilibrium, the electron and hole occupation probabilities are given by the Fermi-Dirac distribution $f(\varepsilon)$. In the presence of an electrical voltage V , the distribution function becomes

$$\hat{h} = \text{diag}(t_+, t_+, t_-, t_-), \quad (12)$$

where

$$t_{\pm} = \tanh\left(\frac{1.76}{T/T_c} \cdot \frac{\varepsilon/\Delta_0 \pm |e|V/\Delta_0}{2}\right). \quad (13)$$

A temperature gradient in a superconductor interfaced with two reservoirs is modeled by setting the temperature in the reservoirs to different values. Similarly, a voltage bias ΔV is modeled by setting the voltage to $+\Delta V/2$ in one reservoir and $-\Delta V/2$ in the other reservoir.

The superconductor is coupled to the normal reservoirs with spin-active boundary conditions [17, 18]:

$$\check{g} \frac{\partial}{\partial(x/\xi)} \check{g} = \frac{\pm G_0/G}{2l/\xi} \left[\check{g}, \check{g} + \frac{G_1}{G_0} \check{m} \check{g} \check{m} + \frac{G_{MR}}{G_0} \{\check{g}, \check{m}\} - i \frac{G_{\varphi}}{G_0} \check{m}' \right]. \quad (14)$$

Here, the + sign is valid at the interface where the reservoir is to the right of the superconductor, and the - sign is valid at the other interface. The Green function in the reservoir is given by \check{g} . In the normal state, $\hat{g}^R = \hat{\rho}_4$ and the distribution function is given by eq. (12). The interface magnetization is described by the unit vector \mathbf{m} , and it enters the magnetization matrix \check{m} as $\check{m} = \hat{1} \otimes \text{diag}(\mathbf{m} \cdot \boldsymbol{\sigma}, \mathbf{m} \cdot \boldsymbol{\sigma}^*)$. The difference between \check{m} and \check{m}' is that they refer to the average magnetization felt by a quasiparticle transmitted and reflected through the interface, respectively. We assume that $\check{m} = \check{m}'$. The conductances in the boundary conditions are interpreted as follows. G_0 is the tunneling conductance, G_1 is a depairing term, G_{MR} is a magnetoresistive term and G_{φ} is the spin-mixing term. Under the assumption that all scattering channels have the same polarization P , then

$$\frac{G_1}{G_0} = \frac{1 - \sqrt{1 - P^2}}{1 + \sqrt{1 - P^2}}, \quad \frac{G_{MR}}{G_0} = \frac{P}{1 + \sqrt{1 - P^2}}. \quad (15)$$

The spin-mixing term can be regarded as a fitting parameter.

When the Usadel equation is solved, we can calculate observables such as the charge current,

$$I = -I_0 \int_0^{\infty} \text{Re Tr} \left[\hat{\rho}_4 \left(\check{g} \frac{\partial \check{g}}{\partial(x/\xi)} \right)^K \right] d\left(\frac{\varepsilon}{\Delta_0}\right), \quad (16)$$

and the superconducting order parameter,

$$\frac{\Delta}{\Delta_0} = -\frac{N_0\lambda}{4} \int_{-\omega_c}^{\omega_c} \hat{g}_{23}^K \left(\frac{\varepsilon}{\Delta_0}\right) d\left(\frac{\varepsilon}{\Delta_0}\right). \quad (17)$$

For eq. (17) to be consistent, the coupling constant λ is related to the cutoff energy by $\omega_c = \cosh(1/N_0\lambda)$. N_0 is the normal-state density of states at the Fermi level. The order parameter enters the Usadel equation as a fixed self-energy, but it can also be calculated from the Green function. Since these values should be consistent, the Usadel equation must be solved by fixed-point iterations. The voltage induced by a temperature gradient is found by solving the root-finding problem $I(\Delta V) = 0$. We finally note that when a voltage and temperature gradient are simultaneously present, the phase of the order parameter drifts when performing fixed point iterations. This means that at each iteration, a constant value is added to the phase at all positions. Nevertheless,

physical observables depend only on the gap $|\Delta|$ and the phase gradient $\partial_x \phi \equiv \partial \phi / \partial(x/\xi)$, which do converge. Therefore, the drift of the phase has no physical meaning. The convergence criteria for the order parameter are chosen to be

$$\frac{||\Delta|_n - |\Delta|_{n-1}|}{|\Delta|_n} < 10^{-5}, \quad \frac{|\partial_x \phi_n - \partial_x \phi_{n-1}|}{\partial_x \phi_n} < 10^{-2}, \quad (18)$$

where n refers to iteration number.

-
- [1] C Tiusan, F Greullet, M Hehn, F Montaigne, S Andrieu, and A Schuhl, “Spin tunnelling phenomena in single-crystal magnetic tunnel junction systems,” *J. Phys.: Condens. Matter* **19**, 165201 (2007).
- [2] César González-Ruano, Diego Caso, Jabir Ali Ouassou, Coriolan Tiusan, Yuan Lu, Jacob Linder, and Farkhad G. Aliev, “Observation of magnetic state dependent thermoelectricity in superconducting spin valves,” *Phys. Rev. Lett.* **130**, 237001 (2023).
- [3] COMSOL Multiphysics® v. 6.3. www.comsol.com. COMSOL AB, Stockholm, Sweden.
- [4] M. Dixon, F. E. Hoare, T. M. Holden, and D. E. Moody, “The low temperature specific heats of some pure metals (cu, ag, pt, al, ni fe co),” *Proceedings of the Royal Society of London. Series A, Mathematical and Physical Sciences* **285**, 561–580 (1965).
- [5] J. W. Gardner and A. C. Anderson, “Effect of neutron irradiation on the low-temperature specific heat and thermal conductivity of magnesium oxide,” *Phys. Rev. B* **23**, 1988–1991 (1981).
- [6] Jung Wayne Douglas, *The thermal conductivity of high purity vanadium*, Ph.D. thesis, Iowa State University (1975).
- [7] Ray Radebaugh and P. H. Keesom, “Low-temperature thermodynamic properties of vanadium. i. superconducting and normal states,” *Phys. Rev.* **149**, 209–216 (1966).
- [8] Isidoro Martínez, Coriolan Tiusan, Michel Hehn, Mairbek Chshiev, and Farkhad G. Aliev, “Symmetry broken spin reorientation transition in epitaxial mgo/fe/mgo layers with competing anisotropies,” *Scientific Reports* **8**, 9463 (2018).
- [9] C. D. Graham, “Magnetocrystalline anisotropy constants of iron at room temperature and below,” *Phys. Rev.* **112**, 1117–1120 (1958).
- [10] J. C. Slonczewski, “Conductance and exchange coupling of two ferromagnets separated by a tunneling barrier,” *Phys. Rev. B* **39**, 6995–7002 (1989).
- [11] L. P. Gorkov, “On the energy spectrum of superconductors,” *Sov. Phys. JETP* **34**, 505–508 (1958).
- [12] W. Belzig, F. K. Wilhelm, C. Bruder, G. d. Schön, and A. D. Zaikin, “Quasiclassical Green’s function approach to mesoscopic superconductivity,” *Superlatt. Microstruct.* **25**, 1251–1288 (1999).
- [13] Venkat Chandrasekhar, “Superconductivity: Conventional and unconventional superconductors,” (Springer, Berlin, 2008) Chap. 8, pp. 279–313.
- [14] Gert Eilenberger, “Transformation of Gorkov’s equation for type II superconductors into transport-like equations,” *Z. Phys.* **214**, 195–213 (1968).
- [15] Klaus D. Usadel, “Generalized diffusion equation for superconducting alloys,” *Phys. Rev. Lett.* **25**, 507–509 (1970).
- [16] N. M. Chtchelkatchev, T. I. Baturina, A. Glatz, and V. M. Vinokur, “Physical Properties of Nanosystems: Synchronized Andreev transmission in chains of SNS junctions,” (Springer, Yalta, 2009) Chap. 7, pp. 87–107.
- [17] M. Eschrig, A. Cottet, W. Belzig, and J. Linder, “General boundary conditions for quasiclassical theory of superconductivity in the diffusive limit: Application to strongly spin-polarized systems,” *New J. Phys.* **17**, 083037 (2015).
- [18] Jabir Ali Ouassou, Tom Doekle Vethaak, and Jacob Linder, “Voltage-induced thin-film superconductivity in high magnetic fields,” *Phys. Rev. B* **98**, 144509 (2018).